Available online at www.sciencedirect.com
ScienceDirect
Trans. Nonferrous Met. Soc. China 34(2024) 3344−3357
Transactions of Nonferrous Metals Society of China
www.tnmsc.cn

Enhancing Na^+ diffusion dynamics and structural stability of O3-$NaMn_{0.5}Ni_{0.5}O_2$ cathode by Sc and Zn dual-substitution

Bin-bin WANG[1], Yi-ming FENG[2], Xin LUO[1], Qun HUANG[3], Zi-xing HOU[1],
Ya-qin WU[1], Peng-yu WANG [1], Yu-yang QI[4], Qing-fei MENG[4], Wei-feng WEI[1], Liang-jun ZHOU[1]

1. State Key Laboratory of Powder Metallurgy, Central South University, Changsha 410083, China;
2. Vital Material Co., Ltd., Guangzhou 510623, China;
3. The 48th Research Institute of China Electronics Technology Group Corporation, Changsha 410111, China;
4. Wuhan Zhongyuan Changjiang Technology Development Co., Ltd., Wuhan 430090, China

Received 29 June 2024; accepted 26 September 2024

Abstract: Sc and Zn were introduced into O3-$NaMn_{0.5}Ni_{0.5}O_2$ (NaMN) using the combination of solution combustion and solid-state method. The effect of Sc and Zn dual-substitution on Na^+ diffusion dynamics and structural stability of NaMN was investigated. The physicochemical characterizations suggest that the introduction of Sc and Zn broaden Na^+ diffusion channels and weaken the Na—O bonds, thereby facilitating the diffusion of sodium ions. Simulations indicate that the Sc and Zn dual-substitution decreases the diffusion barrier of Na-ions and improves the conductivity of the material. The dual-substituted $NaMn_{0.5}Ni_{0.4}Sc_{0.04}Zn_{0.04}O_2$ (NaMNSZ44) cathode delivers impressive cycle stability with capacity retention of 71.2 % after 200 cycles at 1*C* and 54.8% after 400 cycles at 5*C*. Additionally, the full cell paired with hard carbon anode exhibits a remarkable long-term cycling stability, showing capacity retention of 64.1% after 250 cycles at 1*C*. These results demonstrate that Sc and Zn dual-substitution is an effective strategy to improve the Na^+ diffusion dynamics and structural stability of NaMN.

Key words: layered oxide cathode; Sc and Zn dual-substitution; structural stability; Na^+ diffusion dynamics

1 Introduction

The ever-growing demand for portable devices and electric vehicles has contributed to the tremendous success of lithium-ion batteries (LIBs) [1,2]. However, the scarcity and uneven geographical distribution of lithium resources limit future development of LIBs [3,4]. Sodium-ion batteries (SIBs) have recently attracted extensive attention, and are expected to emerge as a promising alternative in the field of new energy storage system. Despite a similar “racking-chair” mechanism to LIBs, SIBs offer the advantages of cost-effectiveness and abundant resources [5,6]. As one of the critical factors in governing the electrochemical performance of SIB, suitable cathode materials is essential for the commercial application of SIBs [7,8]. Among kinds of candidates, including layer transition metal oxides (Na_xTMO_2), polyanionic compounds, prussian blue analogs and organics [9,10], Na_xTMO_2 is recognized as the most promising cathode material, because of their abundant source, environmental friendliness, simplicity of preparation, and excellent electrochemical performance [11,12]. Compared to the Na-poor P2 phase, the Na-rich O3 phase layered oxide has a higher content of sodium and resulting

---

Corresponding author: Qing-fei MENG, Tel: +86-27-65522212, E-mail: mqf2161@qq.com;
Liang-jun ZHOU, Tel: +86-731-88877186, E-mail: alexander-zhou@csu.edu.cn

DOI: 10.1016/S1003-6326(24)66612-4

higher specific capacity in the full cell, thereby indicating its superior potential for commercialization [13].

Typical O3-type Ni/Mn-based layer oxide $NaMn_{0.5}Ni_{0.5}O_2$ (NaMN) delivers high specific capacity and average discharge voltage, which is very attractive in large-scale energy storage field [14]. However, it still suffers from problems associated with multiple phase transitions and sluggish Na^+ transport kinetics [15,16]. On the one hand, during Na^+ de/intercalation, TMO_2 slabs undergo slip-induced irreversible phase transitions, resulting in a volumetric change that can lead to cracks in the grains and capacity degradation [17,18]. On the other hand, the sluggish dynamics and compromised rate performance can be attributed to the large radius (1.02 Å) of sodium and the strong potential barrier that hinders diffusion of sodium ions in the O3 phase [19]. In the past years, many strategies, including structure fabrication [20], surface modification [21] and ions substitution [22], have been developed for overcoming these obstacles. Cation substitution, allowing the formation of robust TM—O bonds and playing a crucial role in structural stability, has been considered as an effective pathway [23,24]. For instance, HU et al [25] proved that Sn^{4+} partially replacing Mn^{4+} could inhibit the irreversible multi-phase transitions, enhance the structural stability and stabilize the anion redox reaction. PENG et al [26] found that the Al^{3+} doping in $NaMn_{0.5}Ni_{0.5}O_2$ could alter the local chemical environment, suppress the complicated phase transitions and decrease the Na^+ diffusion energy barrier. In addition, Li^+ [27], K^+ [28], Mg^{2+} [29], Zn^{2+} [30], Cu^{2+} [31], and Ti^{4+} [32] etc. have been proven to mitigate phase transitions and enhance electrochemical performance. However, single-element doping is limited in terms of improvement [33]. Co-doping of multiple elements can overcome the limitations due to synergistic effect, further improving the structural stability and electrochemical performance of layered oxides [34].

Hence, in this work, Sc and Zn were introduced into NaMN using the combination of solution combustion and solid-state method. And we investigate the effect of Sc and Zn dual-substitution on Na^+ diffusion dynamics and structural stability of NaMN. It is noteworthy that the introduction of Sc into layered oxides is reported for the first time. Due to the special all-vacancy ($3d^0$) extra-nuclear electron arrangement of Sc for reducing lattice distortions [35] and disruption of Zn for Na^+/ vacancy ordering [36], the bonding energy of Sc—O (671 kJ/mol) is much stronger than that of Mn—O (402 kJ/mol) and Ni—O (391.6 kJ/mol), indicating its ability for enhancing the structural stability and cyclability. Meanwhile, introduction of Zn can disrupt the Na^+/vacancy ordering and reduce the potential barrier of Na^+ diffusion, which has a significant impact on the rate performance. Therefore, the dual substitution cathode exhibited impressive capacity retention of 54.8% at 5*C* after 400 cycles. Thus, the combined effect of these two elements offers a promising avenue for material design in achieving high-performance SIBs.

2 Experimental

2.1 Materials synthesis

The O3-$NaMn_{0.5}Ni_{0.5}O_2$ (NaMN), $NaMn_{0.5}Ni_{0.44}Sc_{0.04}O_2$ (NaMNS4), $NaMn_{0.5}Ni_{0.46}Zn_{0.04}O_2$ (NaMNZ4), $NaMn_{0.5}Ni_{0.4}Sc_{0.04}Zn_{0.04}O_2$ (NaMNSZ44) and $NaMn_{0.5}Ni_{0.3}Sc_{0.08}Zn_{0.08}O_2$ (NaMNSZ88) were synthesized via the combination of solution combustion and solid-state method. Specifically, stoichiometric amounts of $C_4H_6MnO_4\cdot 4H_2O$, $C_4H_6NiO_4\cdot 4H_2O$, $Sc(NO_3)_3\cdot xH_2O$, $C_4H_6O_4Zn\cdot 2H_2O$ and $NaNO_3$ (5% excess to compensate the volatilization of sodium during sintering process) were dispersed in 40 mL of deionized water and stirred for 6 h until completely dissolved. Then, the mixed solution was stirred and heated at 80 °C to remove excess water through evaporation, resulting in the formation of a gel. The gel underwent a combustion reaction to obtain fluffy precursor. After grinding, the powder precursor was calcined at 450 °C for 5 h at a heating rate of 1 °C/min, followed by heating to 850 °C for 20 h at a heating rate of 5 °C/min. Then, the material was cooled down to 150 °C in the furnace for eliminating any interference of water and carbon dioxide in the air on the material. Finally, all the samples were preserved in an argon-filled glove box.

2.2 Characterization

X-ray diffraction (XRD) measurements were conducted to characterize the crystal structure on a

Rigaku SmartLab SE diffractometer with Cu K_α radiation in the 2θ range of 10°−80°. The XRD data were further refined by the GSAS and EXPGUI software based on the Rietveld method to analyze the lattice parameters. The morphologies of the samples were observed by scanning electron microscopy (SEM, JSM−7610FPlus, JEOL). Furthermore, Transmission electron microscopy (TEM, JEM−F200, JEOL) equipped with energy-dispersive X-ray spectrometer (EDS, Ultim Max 80) was utilized to investigate the microstructural information and elemental distribution. High angle annular dark field scanning TEM (HAADF-STEM) were conducted by a Double Corrected TEM Spectra 300 (Thermo Fisher Scientific). X-ray photoelectron spectroscopy (XPS, PHI VersaProbe 4, ULVAC-PHI) was used to detect the valence states of the elements on the surface. Inductively coupled plasma atomic emission spectrometry (ICP-OES, ICAP 7000 SERIES) was carried out to determine the specific compositions for different cathode materials.

2.3 Electrochemical measurements

The cathode material, super P and polyvinylidene fluoride (PVDF) were mixed in a mass ratio of 8:1:1 and then dissolved in *N*-methyl pyrrolidone (NMP) solvent. After well dispersed, the slurry was homogeneously cast onto aluminum foil and dried at 110 °C for 12 h in a vacuum oven. The coated foil was then punched into disc electrodes with 12 mm in diameter and the average loading of active material was 1−2 mg/cm^2. The preparation of hard carbon (HC) anode is the same as that of cathode, except that the active material is replaced with hard carbon. The N/P mass ratio was controlled at about 1.2:1 in this work. In an argon-filled glove box, the prepared cathodes were assembled with hard carbon anode and sodium metal in CR-2016 coin cell as half and full cell, respectively. The fiber (Whatman, GF/F) was applied to separating positive and negative electrodes. The electrolyte was a solution of 1 mol/L $NaPF_6$ dissolved in propylene carbonate (PC) with 5 vol.% fluorinated ethylene carbonate (FEC). The pre-sodiation was achieved by placing the hard carbon anode electrode in direct contact with the sodium metal in the electrolyte overnight. Galvanostatic charge−discharge tests were conducted at room temperature in the voltage ranges of 2.0−4.0 V and 2.0−4.2 V (1*C*=200 mA/g) on a NEWARE battery test equipment. Cyclic voltammetry (CV) measurements were conducted using an Arbin electrochemical workstation (BT2000) in the voltage range of 2.0−4.2 V at a scan rate of 0.1 mV/s. Galvanostatic intermittent titration technique (GITT) were utilized to estimate the diffusion coefficient of sodium-ion. For the full cell, the galvanostatic charge−discharge tests was performed in the voltage window of 1.2−4.2 V at room temperature.

2.4 Density functional theory calculation

The first-principles calculations were performed in the framework of the density functional theory (DFT) with the projector augmented plane-wave method, as implemented in the Vienna ab initio simulation package (VASP). The generalized gradient approximation of Perdew, Burke, and Ernzerhof (PBE) is employed for the exchange-correlation potential. The long range vander Waals interaction is described by the DFT-D3 approach. A Hubbard-U term is employed to treat the strongly correlated d-electrons of Ni and Mn atoms. The U parameters were taken from reference, and the values were adopted as 6.3 and 4.95 for Ni and Mn, respectively. The plane-wave basis with a kinetic energy cutoff of 500 eV and the Monkhorst−Pack scheme with a *k*-point grid spacing of $2\pi\times0.05$ Å^{-1}, were employed to ensure the convergence of total energy. The converged conditions for ionic and electronic optimizations were chosen as 0.03 eV/Å and 1×10^{-5} eV, respectively. For the $NaNi_{0.5}Mn_{0.5}O_2$ and $NaNi_{0.42}Mn_{0.5}Zn_{0.04}Sc_{0.04}O_2$ structure, the calculation was based on the supercell obtained by $2\times2\sqrt{3}\times1$ expansion of the conventional cells. The Na^+ diffusion corresponded to single Na migration between two neighboring sites after removing a Na atom. The Na diffusion energy barrier was calculated using the climbing image nudged elastic band method (cNEB).

3 Results and discussion

3.1 Materials characterization

To evaluate the effect of Sc and Zn dual-substitution on NaMN materials, different substituting ratios (4% Zn; 4% Sc; 4% Sc and 4% Zn; 8% Sc and 8% Zn) were attempted. ICP-OES was carried out to determine the specific compositions for different cathode materials. The elemental ratios of all chemical components are consistent with the experimental design components within the permissible error range (Table S1 in Supporting Information (SI)). The crystal structures were characterized by XRD. As shown in Fig. S1 in SI, the diffraction peaks of all samples are in good agreement with α-$NaFeO_2$ layered structure with a space group $R\overline{3}m$ (PDF# 54-0887) [37]. Apparently, the XRD patterns of all the samples show tiny peaks around 2θ=38° and 43°, which can be corresponded to NiO. This arises from the limited solubility of nickel in the O3 phase, leading to the precipitation of some nickel as the NiO impurities during the sintering process [38]. With the increase of Sc and Zn content, the (003) peak gradually shifts toward a lower Bragg angle, which means that an expansion of d-spacing based on the Bragg equation [39].

Besides, to learn more about the change of the lattice parameters after Sc and Zn dual-substitution, the XRD data were further refined by the GSAS software (Figs. 1(a, b)), while the detailed lattice parameters calculated by the Rietveld method are summarized in Tables S2 and S3 in SI. The errors obtained from the refinement are all within reasonable limits, suggesting the credibility of the refinement data. The occupancy value of nickel decreases with Sc and Zn dual-substitution, indicating successful incorporation of Sc and Zn elements into the lattice and replacement of Ni sites. The lattice parameters a, c and V of NaMNSZ44 expand upon Sc and Zn dual-substitution compared with those of the pristine NaMN, which can be attributed to the fact that the ionic radius of Sc^{3+} (0.745 Å) and Zn^{2+} (0.74 Å) is larger than that of Mn^{4+} (0.53 Å) and Ni^{2+} (0.69 Å), resulting in lattice expansion. The expansion of c-axis leads to an increase in the sodium layer spacing, which is conducive to improving the diffusion of Na^+ [40]. Meanwhile, the stronger bond energy of Sc—O (671 kJ/mol) can enhance crystal structure stability and inhibit the multi-phase transition due to the slip

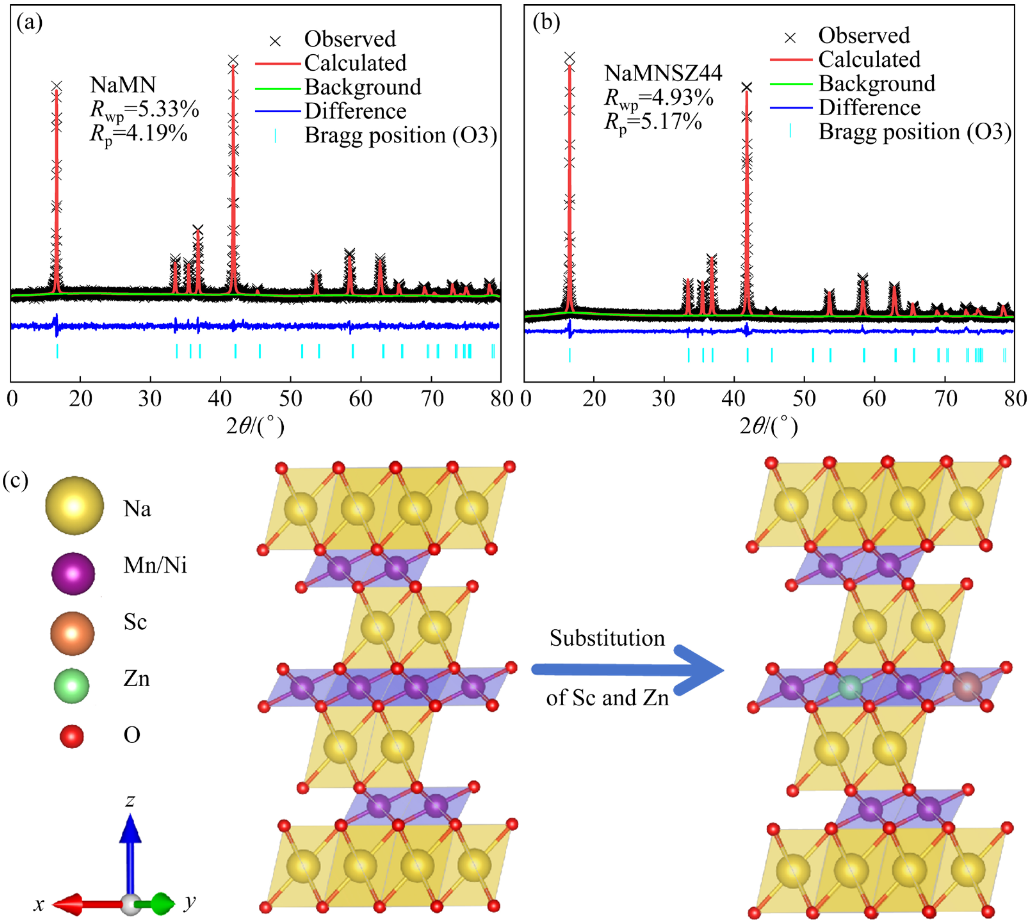

Fig. 1 XRD Rietveld refinement patterns of NaMN (a) and NaMNSZ44 (b); Schematic diagrams of crystal structure model of NaNM and NaMNSZ44 (c)

of the transition metal layers [35]. Figure 1(c) shows the schematic diagrams of crystal structure model of NaMN and NaMNSZ44.

The SEM images of samples are shown in Figs. 2(a, b) and Fig. S2 in SI, demonstrating the presence of a flat-like morphology. The observed morphology is common in high-temperature solid-phase synthesis for typical layered cathode materials. It is worth noting that the particle size of NaMNSZ44 sample appears to be larger than that of NaMN, indicating that the introduction of Sc and Zn elements can facilitate crystal growth during sintering process. The decrease in specific surface area is conducive to boost air stability and diminish potential for side reactions with the electrolyte [41]. The HAADF-STEM images of NaMN and NaMNSZ44 samples (Figs. 2(c, d)) exhibit clear layered structure and good crystallinity. An increase of the layer space from 0.554 nm in NaMN to 0.567 nm in NaMNSZ44 can be observed, which is corresponded to the shift of (003) peak in the XRD patterns. Additionally, to demonstrate the homogeneity of the Sc and Zn dual-substitution, the energy-dispersive X-ray spectrometer (EDS) was utilized to measure the distribution of Na, Mn, Ni, Sc and Zn (Fig. S3 in SI). The results show that all elements are evenly distributed in the particles.

3.2 Charge compensation mechanism

To identify the influence of Sc and Zn introduction on the valence states of different elements in the cathode materials, XPS technique was employed on NaMN and NaMNSZ44 samples. Figure 3(a) demonstrates that the peak of Na 1s exhibits a shift towards lower binding energy, which suggests the weakening of Na—O bond. The Sc $2p_{1/2}$ and Sc $2p_{3/2}$ peaks are observed at 399.6 and 404 eV (Fig. 3(b)), respectively, which is corresponded to the Sc^{3+} state [42]. In Fig. 3(c), the NaMNSZ44 sample exhibits the energy levels at 1018.9 and 1041.9 eV, indicating the presence of the Zn element, and the valence state of Zn is +2 [43]. As shown in Figs. 3(d, e), valence states of Mn and Ni are present in both samples as +3 and +4, and +2 and +3, respectively. Gaussian fitting was performed to confirm the ratio of Mn^{3+} to Mn^{4+} and Ni^{2+} to Ni^{3+} in the two samples. The proportion of Mn^{3+} decreases from 63.51% in NaMN to 56.66% in NaMNSZ44, which could attenuate the Jahn−Teller effect for the structure. Meanwhile, the proportion of Ni^{2+} decreases from 35.07% in NaMN to 33.67% in NaMNSZ44. The reduction in the proportion of Ni^{2+} and Mn^{3+} can be ascribed to the introduction of Sc^{3+} and Zn^{2+}, which breaks the charge conservation. In order to maintain the

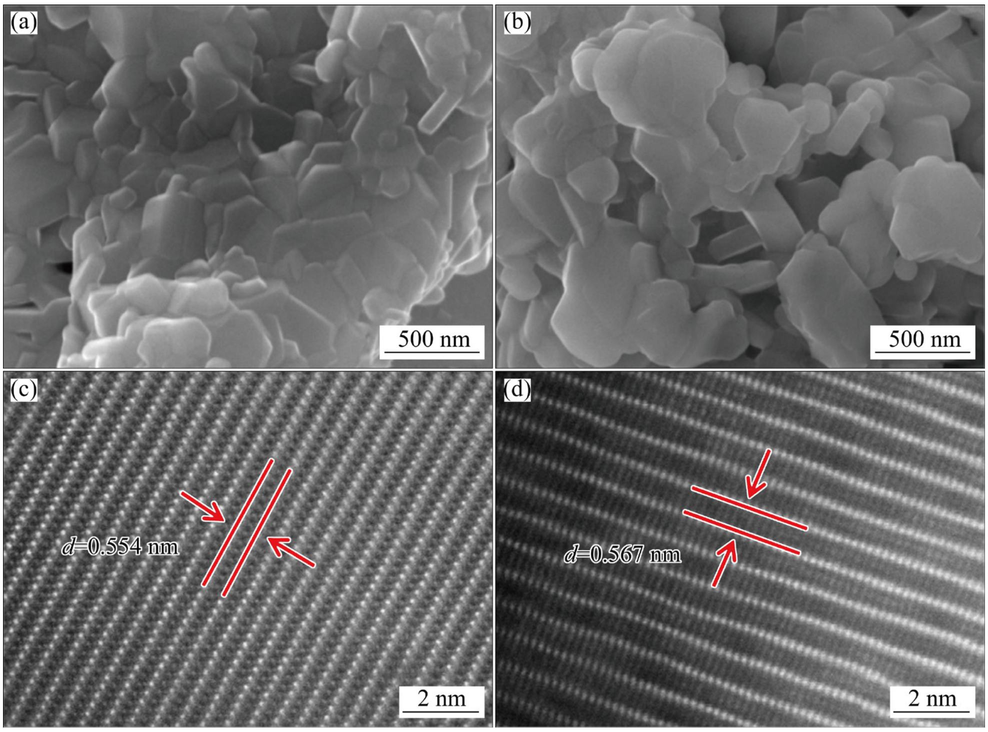

Fig. 2 SEM images of particles for NaMN (a) and NaMNSZ44 (b); HAADF-STEM images of NaMN (c) and NaMNSZ44 (d)

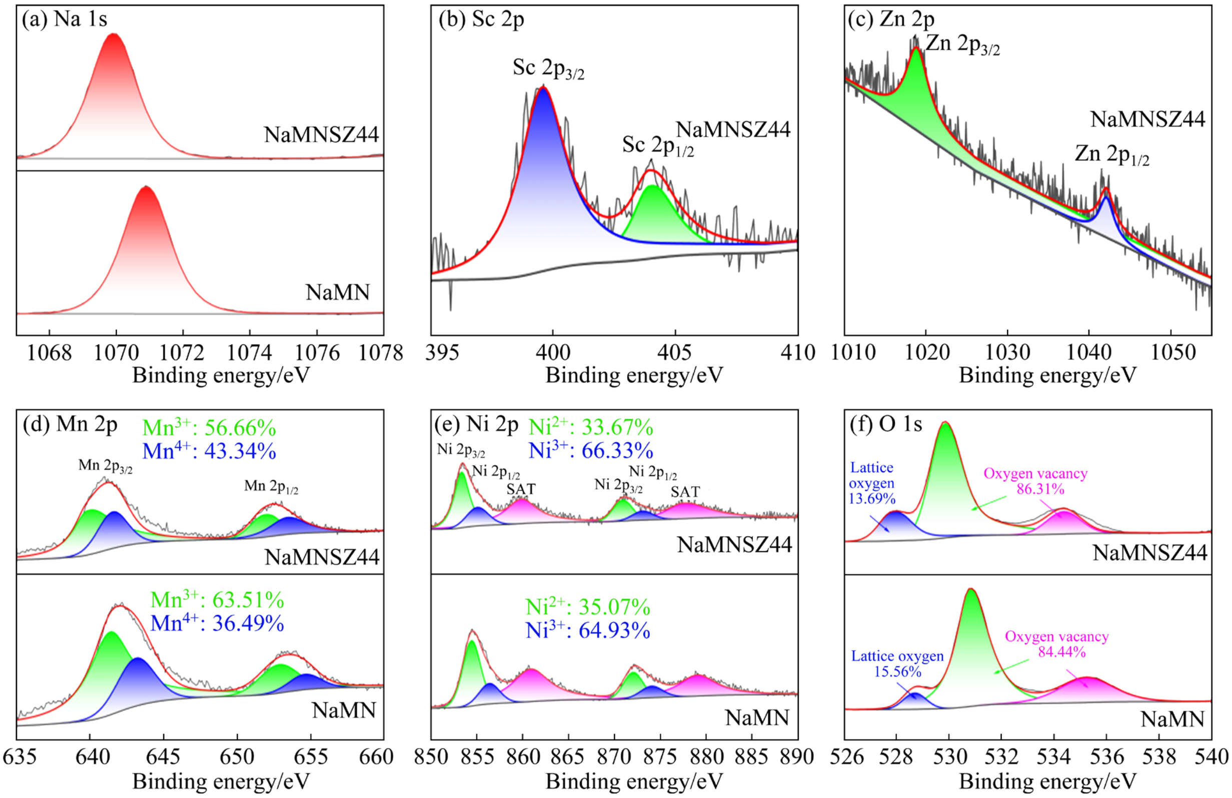

Fig. 3 XPS spectra of Na 1s (a), Sc 2p (b), Zn 2p (c), Mn 2p (d), Ni 2p (e) and O 1s (f) in NaMN and NaMNSZ44

equilibrium, and considering that the valence states of Sc and Zn remain constant, the Ni^{2+} and Mn^{3+} contents decrease whereas the Ni^{3+} and Mn^{4+} contents increase. The change in chemical properties of oxygen before and after the substitution is compared in Fig. 3(f). Generally, oxygen exists in two forms, namely lattice oxygen and loose oxygen. The ratios of the lattice oxygen and loose oxygen vacancies in both samples were calculated by Gaussian fitting, suggesting a partial escape of oxygen from the lattice in NaMNSZ44, and correspondingly more oxygen vacancies are generated.

3.3 Theoretical calculation of Sc and Zn dual-substituted oxide compounds

To deeply investigate the role of Sc and Zn dual-substitution on diffusion barrier of Na-ions, density functional theory (DFT) calculations were conducted to obtain Na-ions diffusion energy barriers in NaMN and NaMNSZ44. The results (Figs. 4(a, b)) show that the diffusion barrier for Na-ions in NaMNSZ44 (1.562 eV) is lower than that in NaMN (1.661 eV). Figure 4(c) illustrates the Na-ions diffusion path for the NaMNSZ44. Na-ions preferentially diffuse in two dimensions between the TMO layers in both structures.

Furthermore, the total densities of states (tDOS) for NaMN and NaMNSZ44 are shown in Figs. 4(d, e). Since the electron transfer is mainly compensated by the oxidative reduction of Ni ions, the electronic states of the Ni 3d and O 2p orbitals predominate the electronic states near the Fermi level [44]. The forbidden bandwidths of the spin-up and spin-down state densities of NaMN are 0.111 and 3.179 eV, respectively, while the total forbidden bandwidth is 0.111 eV. For NaMNSZ44, there is no bandgap in the spin-down state density, suggesting that metallic features are formed [45]. This is due to the significant reduction of the energy band after Sc and Zn dual-substitution. It can be deduced that the conductivity can increase in NaMNSZ44, which is further proven in the electrochemical performances. The results of simulations are in good agreement with the XPS data.

3.4 Electrochemical performance

The electrochemical performances of samples were evaluated by assembling sodium-ion half-cells with metal sodium as the counter electrode. The charge/discharge curves of samples during the initial three cycles at a rate of 0.1C (1C=200 mA/g)

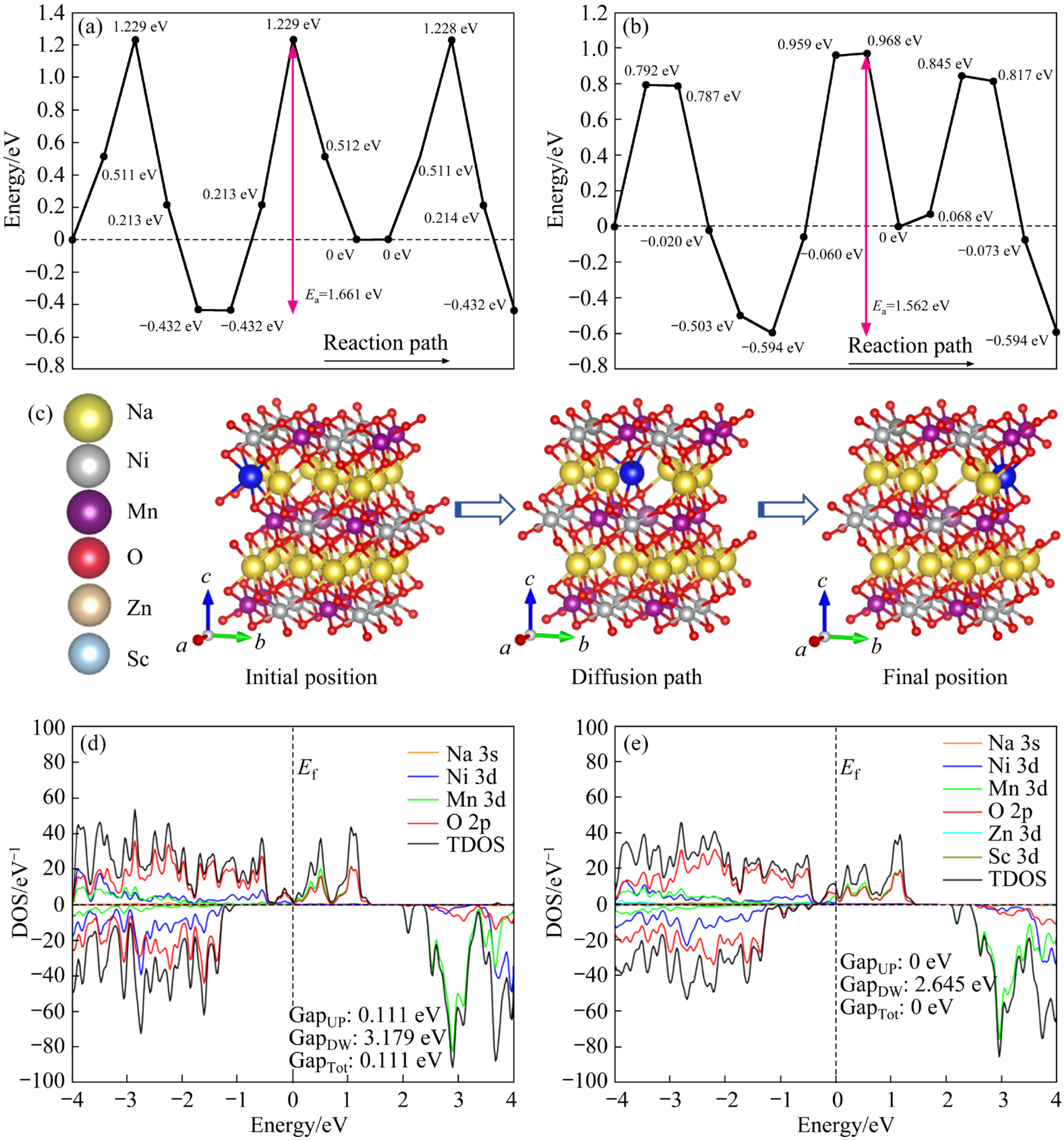

Fig. 4 Na-ion diffusion energy barriers in NaMN (a) and NaMNSZ44 (b); Na-ion diffusion pathways in NaMNSZ44 (c); Total densities of states for NaMN (d) and NaMNSZ44 (e)

at 2.0−4.2 V are displayed in Figs. 5(a, b) and Fig. S4 in SI. The loss of initial discharge capacity is due to the introduction of inactive elements of Sc and Zn. It can be seen that the curve of NaMNSZ44 is smoother than that of NaMN. Compared to the curves of NaMN with five voltage plateaus, the curves of NaMNSZ44 have only two voltage plateaus. Three voltage plateaus above 3 V disappear, which is related to Na^+/vacancy ordering and multi-phase transition. Therefore, it can be inferred that the introduction of Sc and Zn may significantly inhabit the irreversible phase transition and disrupt the Na^+/vacancy ordering.

The rate performances from 0.1*C* to 10*C* of samples are compared in Figs. 5(c) and Fig. S5 in SI. With the increase of current density, the NaMNSZ44 exhibits excellent rate performance, maintaining capacities of 151.9, 135.86, 124.62, 114.38, 101, 78.81, 66.14, 60.22 mA·h/g at 0.1*C*, 0.2*C*, 0.5*C*, 1*C*, 2*C*, 5*C*, 8*C* and 10*C*, respectively. Conversely, the discharge capacity of NaMN decays rapidly, especially at high current densities, which is consistent with the results of DFT calculation.

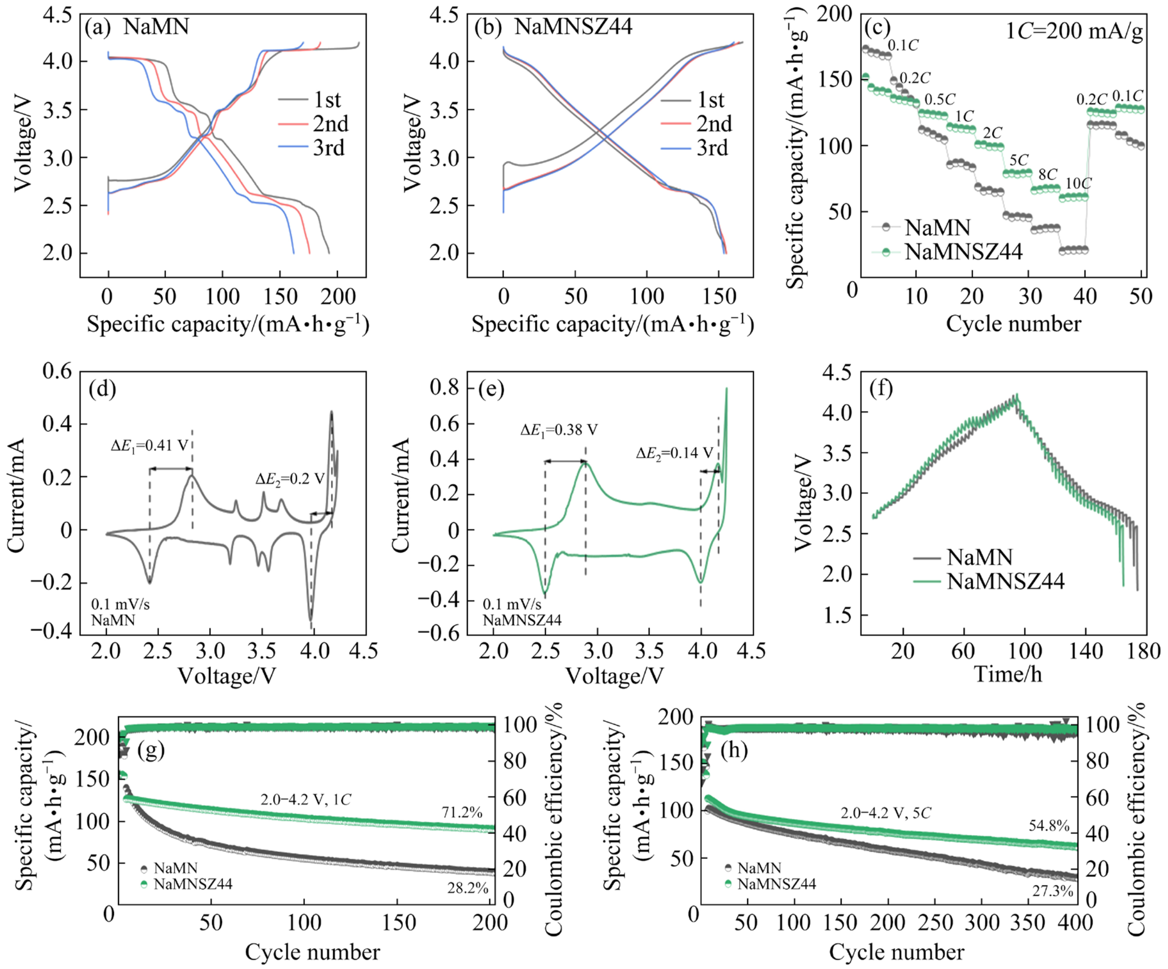

Fig. 5 Initial three-cycle charge−discharge curves of NaMN (a) and NaMNSZ44 (b) at rate of 0.1*C*; Rate performance of two samples at various rates (c); CV profiles for NaMN (d) and NaMNSZ44 (e) at scan rate of 0.1 mV/s; GITT profiles for both samples (f); Long cycle performance at 1*C* (g) and 5*C* (h) for both cathodes

As shown in Figs. 5(d, e), five redox peaks are observed in the CV of NaMN, which are corresponded exactly to the five voltage plateaus in the charge−discharge curves. The first major redox peak around 2.8 V represents the highly reversible O3−P3 phase transition during the charge−discharge process. The polarization potential ΔE_1 of NaMNSZ44 is decreased, which is 0.38 mV for NaMNSZ44 in contrast to 0.41 mV for NaMN. Moreover, the redox peak close to 4.1 V exhibits a lower polarization potential ΔE_2 for the P3−O3′ phase transition. These results above suggest that the polarization is alleviated by Sc and Zn dual-substitution, which can obtain highly reversible electrochemical behaviors and reduce irreversible capacity loss during the Na^+ de/intercalation. The galvanostatic intermittent titration technique (GITT) was performed to measure the Na^+ diffusion coefficient in the voltage range of 2.0−4.2 V (Fig. 5(f)), which have been widely used to calculate the diffusivities of sodium ions [46]. The calculated D_{Na+} values of NaMN and NaMNSZ44 are 3.23×10^{-9} and 5.67×10^{-9} cm^2/s, demonstrating that NaMNSZ44 offers Na^+ dynamics performance superior to that of NaMN.

Figure 5(g) and Fig. S6 in SI display the long cycling performance of samples at 1*C*. The initial discharge capacities of NaMN and NaMNSZ44 are measured at 134.64 and 126.34 mA·h/g. After 200 cycles, the final discharge capacities are observed to be 39.35 and 89.94 mA·h/g, with corresponding capacity retentions of 28.2% and 71.2%. Figure 5(h) further compares the cycling stability of NaMN and NaMNSZ44 at a high current density of 5*C*. After 400 cycles, the NaMNSZ44 exhibits 54.8% capacity retention, whereas NaMN has only 27.3%

capacity retention.

In addition, Fig. S7 in SI compares the electrochemical performance of NaMN and NaMNSZ44 in the narrow voltage window of 2.0−4.0 V. Similarly, the curve of NaMNSZ44 is smoother than that of NaMN, as shown in Fig. S7(a, b). The rate capacities from 0.1*C* to 5*C* are shown in Fig. S7(c). NaMNSZ44 has better rate performances for its larger Na^+ transport channels, which can obtain 125 mA·h/g at 5*C*, higher than 50.97 mA·h/g of NaMN. Figure S7(d) compares the cycle performance of NaMN and NaMNSZ44. It can be seen that the long cycle retention of Sc and Zn dual-substituted cathode materials (80.7%) is much higher than that of pristine materials (25.1%).

In addition to the above remarkable electrochemical performances in sodium half-cell, NaMNSZ44 also exhibits excellent full cell performances, which initially demonstrates the practical commercial viability of the modified cathode. As shown in Figs. 6(a, b), the charge−discharge curves undergo the same changes similar to those of the half-cells. The curves of NaMNSZ44 become smoother and have fewer voltage plateaus, which further proves that the Na^+/vacancy ordering is disrupted. Figure 6(c) displays that following 250 cycles at 1*C*, the NaMNSZ44 delivers the capacity retention from 20.1% to 64.1%. This indicates that Sc and Zn dual-substitution has an effective effect on stability and the NaMNSZ44 has the potential for practical applications.

3.5 Structure evolution

In order to further investigate the structural degradation of the materials after cycling, XRD and SEM analyses were carried out on NaMN and NaMNSZ44 after cycling. The SEM images of both materials in Fig. 7 before cycling and after 100 and 200 cycles suggest that, stepped edges come out on the surface of the primary particles in NaMN after 100 cycles, while macroscopic cracks caused by slippage are clearly observed after 200 cycles. However, there is no obvious interfacial degradation of the particles can be observed in NaMNSZ44, which still retains the plate-like morphology, but the edges become rough.

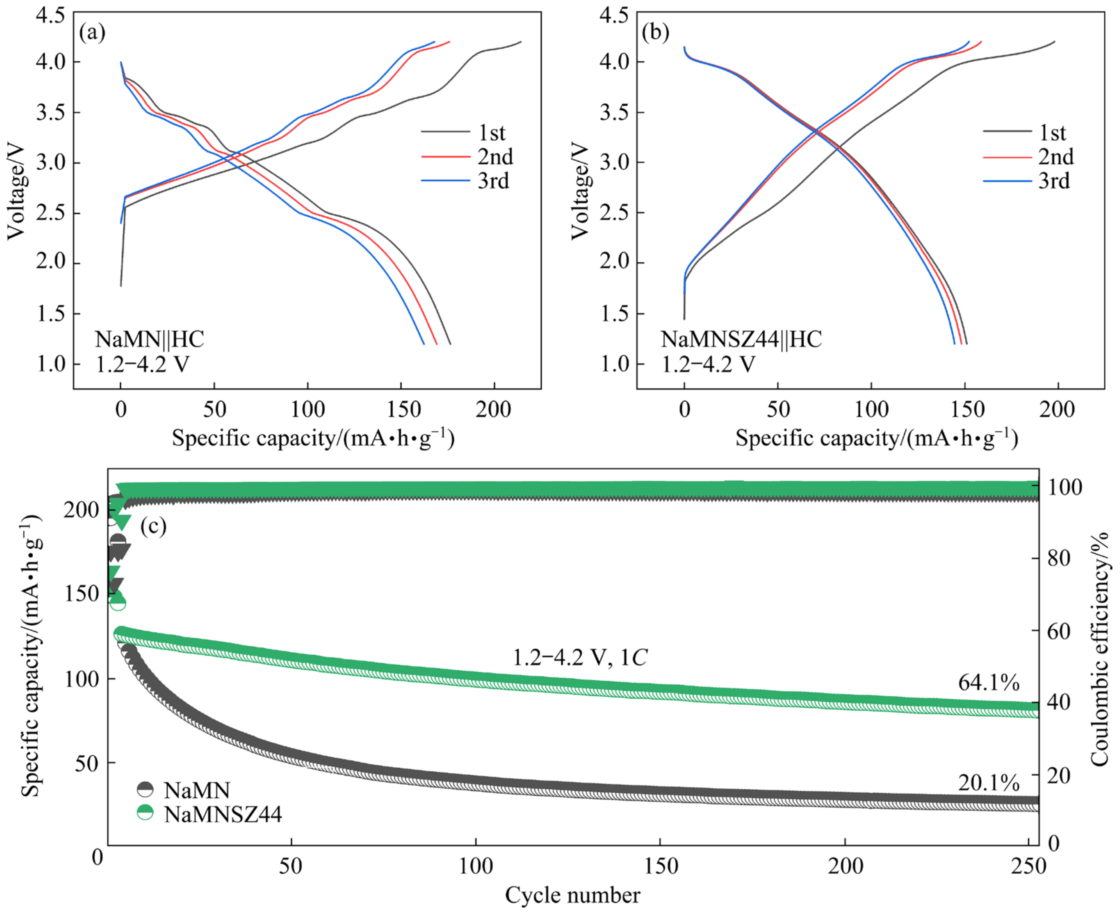

Fig. 6 Electrochemical performances of full-cell tested at 1.2−4.2 V: (a, b) Initial three-cycle charge−discharge curves at 0.1*C*; (c) Long cycle performances at 1*C*

Figures 8(a, b) display the XRD patterns of both materials before cycling and after 100 and 200 cycles. After 200 cycles, the main peaks of (003) and (104) belonging to O3 phase gradually disappear from the XRD spectrum of NaMN electrodes, transforming to the sodium-deficient P3 phase with a larger layer spacing, which indicates the poor structural stability of the NaMN material.

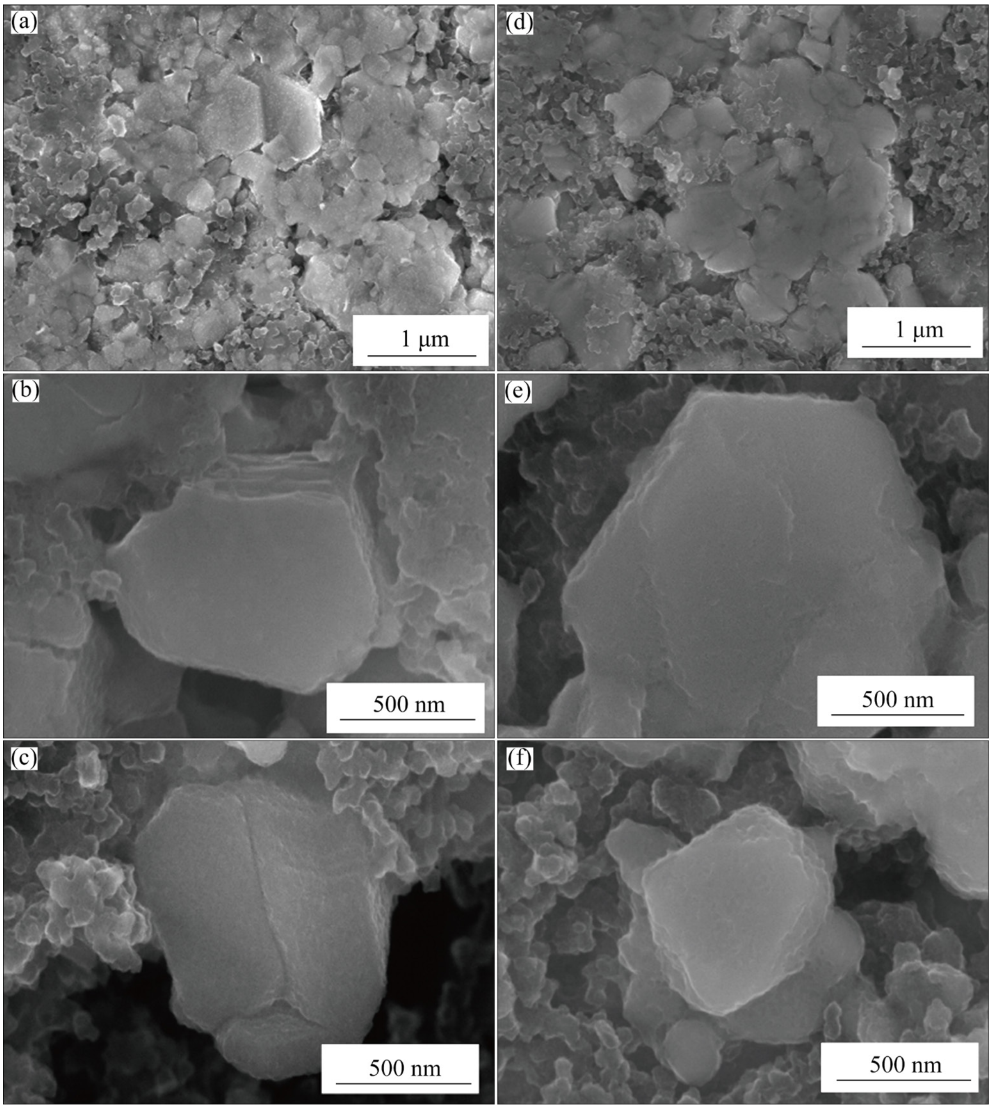

Fig. 7 SEM images of NaMN (a−c) and NaMNSZ44 (d−f) electrodes at initial state (a, d), after 100 (b, d) and 200 (c, f) cycles

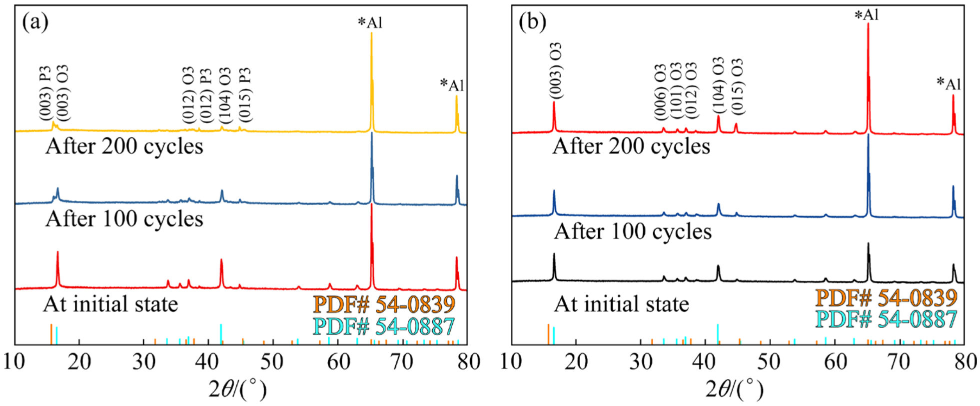

Fig. 8 XRD patterns of NaMN (a) and NaMNSZ44 (b) at initial state, and after 100 and 200 cycles

In contrast, NaMNSZ44 still retains original O3 phase after cycling. This can be attributed to the fact that the substitution of Sc and Zn stabilizes the structure and suppresses the irreversible phase transition.

4 Conclusions

(1) The introduction of Sc and Zn leads to the expansion of the lattice parameters, which is conducive to improving the diffusion of Na^+. The particle size of NaMNSZ44 appears to be larger than that of NaMN, indicating that the material has better air stability and less potential for side reactions with the electrolyte.

(2) The results of the XPS suggest that introduction of Sc^{3+} and Zn^{2+} breaks the charge conservation and leads to changes in the ratio of Mn^{3+} to Mn^{4+} and Ni^{2+} to Ni^{3+}. The reduction of Mn^{3+} can attenuate the Jahn−Teller effect and boost the structural stability.

(3) DFT calculation indicates that the Sc and Zn dual-substitution decreases the diffusion barrier of Na-ions and improves the conductivity of the material.

(4) Electrochemical performance demonstrates that NaMNSZ44 cathode delivers impressive cycle stability. After 200 cycles at 1*C*, NaMNSZ44 exhibits 71.2% capacity retention. NaMNSZ44 delivers 54.8% capacity retention at a high current density of 5*C* after 400 cycles, whereas NaMN has only 27.3%. Additionally, the full cell paired with hard carbon anode still exhibits a remarkable long-term cycling stability, showing capacity retention of 64.1% after 250 cycles at 1*C*.

(5) After cycling, NaMNSZ44 exhibits good structural stability. No obvious interfacial degradation of the particles and changes of structure can be observed in NaMNSZ44.

CRediT authorship contribution statement

Bin-bin WANG: Conceptualization, Data curation, Methodology, Investigation, Writing – Original draft; **Yi-ming FENG:** Formal analysis, Visualization, Software; **Xin LUO:** Validation, Formal analysis, Visualization; **Qun HUANG:** Investigation, Data curation; **Zi-xing HOU:** Investigation, Validation; **Ya-qin WU:** Investigation, Methodology; **Peng-yu WANG:** Visualization; **Yu-yang QI:** Supervision; **Qing-fei MENG:** Conceptualization, Writing − Review & editing; **Wei-feng WEI:** Supervision, Resources; **Liang-jun ZHOU:** Project administration, Conceptualization, Supervision, Writing − Review & editing.

Declaration of competing interest

The authors declare that they have no known competing financial interests or personal relationships that could have appeared to influence the work reported in this paper.

Acknowledgments

The authors would like to acknowledge financial support from the National Natural Science Foundation of China (No. 52377220), and the Natural Science Foundation of Hunan Province, China (No. kq2208265).

Supporting Information

Supporting Information in this work can be found at: http://tnmsc.csu.edu.cn/download/17-p3344-2024-0912-Supporting_Information.pdf.

References

[1] NAYAK P K, YANG Liang-tao, BREHM W, ADELHELM P. From lithium-ion to sodium-ion batteries: Advantages, challenges, and surprises [J]. Angew Chemie International Edition, 2018, 57(1): 102−120.

[2] HOU De-wen, XIA Da-wei, GABRIEL E, RUSSELL J A, GRAFF K, Ren Yang, SUN Cheng-jun, LIN Feng, LIU Yu-zi, XIONG Hui. Spatial and temporal analysis of sodium-ion batteries [J]. ACS Energy Letters, 2021, 6(11): 4023−4054.

[3] HAO Zhi-qiang, SHI Xiao-yan, YANG Zhuo, ZHOU Xun-zhu, LI Lin, MA Chang-qi, CHOU Shu-lei. The distance between phosphate-based polyanionic compounds and their practical application for sodium-ion batteries [J]. Advanced Materials, 2023, 36: 2305135.

[4] ZUO Wen-hua, INNOCENTI L, ZARRABEITIA M, BRESSER D, YANG Yong, PASSERINI S. Layered oxide cathodes for sodium-ion batteries: Storage mechanism, electrochemistry, and techno-economics [J]. Accounts of Chemical Research, 2023, 56(3): 284−296.

[5] ISLAM M S, FISHER A J. Lithium and sodium battery cathode materials: computational insights into voltage, diffusion and nanostructural properties [J]. Chemical Society Reviews, 2014, 43(1): 185−204.

[6] GAO Yun, ZHANG Hang, PENG Jian, LI Lin, XIAO Yao, LI Li, LIU Yang, QIAO Yun, CHOU Shu-lei. A 30-year overview of sodium-ion batteries [J]. Carbon Energy, 2024, 6(6): e464.

[7] CHEN Jing-wei, ADIT G, LI Lun, ZHANG Ying-xin, CHUA H C., LEE P S. Optimization strategies toward functional sodium-ion batteries [J]. Energy & Environmental Materials, 2023, 6(4): e12633.

[8] YIN Wen-ji, SU Pei-dan, LU Qi, LI Xiao-qiong, PENG Ji-ming, ZHOU Teng-fei, LIANG Ge-meng, CAO Yu-liang, WANG Hong-qiang, LI Qing-yu, HU Si-jiang. Ternary-phase

layered cathodes toward ultra-stable and high-rate sodium ion storage [J]. Rare Metals, 2023, 43(4): 1589−1598.

[9] HUANG Zhi-xiong, GU Zhen-yi, HENG Yong-li, ANG Edison Hui-xiang, GENG Hong-bo, WU Xing-long. Advanced layered oxide cathodes for sodium/potassium-ion batteries: Development, challenges and prospects [J]. Chemical Engineering Journal, 2023, 452: 139438.

[10] GAO Han-qing, ZENG Jin-jue, SUN Zhi-peng, JIANG Xiang-fen, WANG Xue-bin. Advances in layered transition metal oxide cathodes for sodium-ion batteries [J]. Materials Today Energy, 2024, 42: 101551.

[11] HUANG Qun, WANG Mei-yu, ZHANG Li, QI Shuo, FENG Yi-ming, HE Ping-ge, JI Xiao-bo, WANG Peng, ZHOU Liang-jun, CHEN Shuang-qiang, WEI Wei-feng. Shear-resistant interface of layered oxide cathodes for sodium ion batteries [J]. Energy Storage Materials, 2022, 45: 389−398.

[12] QIN Mu-lan, YIN Chang-yu, XU Wen, LIU Yang, WEN Jun-hao, SHEN Bin, WANG Wei-gang, LIU Wan-min. Facile synthesis of high capacity P2-type $Na_{2/3}Fe_{1/2}Mn_{1/2}O_2$ cathode material for sodium-ion batteries [J]. Transactions of Nonferrous Metals Society of China, 2021, 31(7): 2074−2080.

[13] YANG Shun-yi, WANG Xian-you, WANG Ying, CHEN Quan-qi, LI Jiao-jiao, YANG Xiu-kang. Effects of Na content on structure and electrochemical performances of $Na_xMnO_{2+\delta}$ cathode material [J]. Transactions of Nonferrous Metals Society of China, 2010, 20(10): 1892−1898.

[14] YU T Y, RYU H H, HAN G, SUN Y K. Understanding the capacity fading mechanisms of O3-type $Na[Ni_{0.5}Mn_{0.5}]O_2$ cathode for sodium-ion batteries [J]. Advanced Energy Materials, 2020, 10(37): 2001609.

[15] ZHOU Chao-jin, YANG Li-chun, ZHOU Chao-gang, LU Bin, LIU Jiang-wen, OUYANG Liu-zhang, HU Ren-zong, LIU Jun, ZHU Min. Co-substitution enhances the rate capability and stabilizes the cyclic performance of O3-type cathode $NaNi_{0.45-x}Mn_{0.25}Ti_{0.3}Co_xO_2$ for sodium-ion storage at high voltage [J]. ACS Applied Materials & Interfaces, 2019, 11(8): 7906−7913.

[16] SAXENA S, BADOLE M, VASAVAN H N, SRIHARI V, DAS A K, GAMI P, DESWAL S, KUMAR P, KUMAR S. Deciphering the role of optimal P2/O3 phase fraction in enhanced cyclability and specific capacity of layered oxide cathodes [J]. Chemical Engineering Journal, 2024, 485: 149921.

[17] XIAO Yao, WANG Peng-fei, YIN Ya-xia, ZHU Yan-fang, YANG Xinan, ZHANG Xu-dong, WANG Yue-sheng, GUO Xiao-dong, ZHONG Ben-he, GUO Yu-guo. A layered-tunnel intergrowth structure for high-performance sodium-ion oxide cathode [J]. Advanced Energy Materials, 2018, 8(22): 1800492.

[18] SONG Xiao-bai, LIU Ruo-nan, JIN Jun-teng, ZHAO Xu-dong, WANG Yao, SHEN Qiu-yu, SUN Zi-qing, QU Xuan-hui, JIAO Li-fang, LIU Yong-chang. Unraveling the functioning mechanism of fluorine-doping in Mn-based layered oxide cathodes toward enhanced sodium-ion storage performance [J]. Energy Storage Materials, 2024, 69: 103377.

[19] WU Lin-rong, ZHANG Yu-han, WU Zhen, TIAN Jin-lv, WANG Hao-rui, ZHAO Hai-jun, XU Shou-dong, CHEN Liang, DUAN Xiao-chuan, ZHANG Ding, GUO Hui-juan, YOU Ya, ZHU Zhi. Stabilized O3-type layered sodium oxides with enhanced rate performance and cycling stability by dual-site Ti^{4+}/K^+ substitution [J]. Advanced Science, 2023, 10(32): 2304067.

[20] LUO Xin, HUANG Qun, FENG Yi-ming, ZHANG Chun-xiao, LIANG Chao-ping, ZHOU Liang-jun, WEI Wei-feng. Constructing a composite structure by a gradient Mg^{2+} doping strategy for high-performance sodium-ion batteries [J]. ACS Applied Materials & Interfaces, 2022, 14(46): 51846−51854.

[21] CHANG Yi-jiao, XIE Guang-hui, ZHOU Yong-mao, WANG Jie-xi, WANG Zhi-xing, GUO Hua-jun, YOU Bian-zheng, YAN Guo-chun. Enhancing storage performance of P2-type $Na_{2/3}Fe_{1/2}Mn_{1/2}O_2$ cathode materials by Al_2O_3 coating [J]. Transactions of Nonferrous Metals Society of China, 2022, 32(1): 262−272.

[22] DANG Yu-zhen, XU Zhe, WU Yu-rong, ZHENG Run-guo, WANG Zhi-yuan, LIN Xiao-pin, LIU Yan-guo, LI Zheng-Yao, SUN Kai, CHEN Dong-feng, WANG Dan. Boron-doped high-entropy oxide toward high-rate and long-cycle layered cathodes for wide-temperature sodium-ion batteries [J]. Journal of Energy Chemistry, 2024, 95: 577−587.

[23] GUO Yu-jie, WANG Peng-fei , NIU Yu-bin, ZHANG Xu-dong, LI Qing-hao, YU Xi-qian, FAN Min, CHEN Wan-ping, YU YANG, LIU Xiang-feng, MENG Qing-hai, XIN Sen, YIN Ya-xia, GUO Yu-guo. Boron-doped sodium layered oxide for reversible oxygen redox reaction in Na-ion battery cathodes [J]. Nature Communications, 2021, 12(1): 5267.

[24] TIAN Yin-feng, CAI Yu-sheng, CHEN Yuan-ping, JIA Min, HU Hao-nan, XIE Wen-yong, LI Dong-ke, SONG Hu-cheng, GUO Shao-hua, ZHANG Xiao-yu. Accessing the O vacancy with anionic redox chemistry toward superior electrochemical performance in O3 type Na-ion oxide cathode [J]. Advanced Functional Materials, 2024, 34(32): 2316342.

[25] HU Hai-yan, WANG Hong-rui, ZHU Yan-fang, LI Jia-YANG, LIU Yi-feng, WANG Jing-qiang, LIU Han-xiao, JIA Xin-bei, LI Hong-wei, SU Yu, GAO Yun, CHEN Shuang-qiang, WU Xiong-wei, DOU Shi-xue, CHOU Shu-lei, XIAO Yao. A universal strategy based on bridging microstructure engineering and local electronic structure manipulation for high-performance sodium layered oxide cathodes [J]. ACS Nano, 2023, 17(16): 15871−15882.

[26] PENG Bo, CHEN Yan-xu, ZHAO Li-ping, ZENG Su-yuan, WAN Guang-lin, WANG Feng, ZHANG Xiao-lei, WANG Wen-tao, ZHANG Gen-qiang. Regulating the local chemical environment in layered O3-$NaNi_{0.5}Mn_{0.5}O_2$ achieves practicable cathode for sodium-ion batteries [J]. Energy Storage Materials, 2023, 56: 631−641.

[27] WANG Qing, MARIYAPPAN S, ROUSSE G, MOROZOV A V, PORCHERON B, DEDRYVERE R, WU Jin-peng, YANG Wan-li, ZHANG Lei-ting, CHAKIR M, AVDEEV M, DESCHAMPS M, YU Y S, CABANA J, DOUBLET M L, ABAKUMOV A M, TARASCON J M. Unlocking anionic redox activity in O3-type sodium 3d layered oxides via Li substitution [J]. Nature Materials, 2021, 20(3): 353−361.

[28] YUAN Tao, SUN Yuan-yuan, LI Si-qing, CHE Hai-ying, ZHENG Qin-feng, NI Yong-jian, ZHANG Yi-xiao, ZOU Jie,

ZANG Xiao-xian, WEI Shi-hao, PANG Yue-peng, XIA Shui-xin, ZHENG Shi-you, CHEN Li-wei, MA Zi-feng. Moisture stable and ultrahigh-rate Ni/Mn-based sodium-ion battery cathodes via K^+ decoration [J]. Nano Research, 2023, 16(5): 6890−6902.

[29] TIAN Jin-Lv, WU Lin-rong, ZHAO Hai-jun, XU Shou-dong, CHEN Liang, ZHANG Ding, DUAN Xiao-chuan. Development of lithium-free P2-type high-sodium content cathode materials with enhanced cycle and air stability for sodium-ion batteries [J]. Rare Metals, 2023, 43(1): 113−123.

[30] MARIYAPPAN S, MARCHANDIER T, RABUEL F, IADECOLA A, ROUSSE G, MOROZOV A V, ABAKUMOV A M, TARASCON J M. The role of divalent $(Zn^{2+}/Mg^{2+}/Cu^{2+})$ Substituents in achieving full capacity of sodium layered oxides for Na-ion battery applications [J]. Chemistry of Materials, 2020, 32(4): 1657−1666.

[31] YAO Hu-rong, WANG Peng-fei, GONG Yue, ZHANG Jie-nan, YU Xi-qian, GU Lin, OUYANG Chu-ying, YIN Ya-xia, HU En-yuan, YANG Xiao-qing, STAVISKI E, GUO Yu-guo, WAN Li-Jun. Designing air-stable O3-type cathode materials by combined structure modulation for Na-ion batteries [J]. Journal of the American Chemical Society, 2017, 139(25): 8440−8443.

[32] HUANG Qun, FENG Yi-ming, XU Sheng, XIAO Lei, HE Ping-ge, JI Xiao-bo, WANG Peng, ZHOU Liang-jun, WEI Wei-feng. A P2@tunnel heterostructure cathode for high-performance sodium-ion batteries [J]. ChemElectroChem, 2020, 7(21): 4383−4389.

[33] HUANG Qun, FENG Yi-ming, WANG Lei, QI Shuo, HE Ping-ge, JI Xiao-bo, LIANG Chao-ping, CHEN Shuang-qiang, ZHOU Liang-jun, WEI Wei-feng. Structure modulation strategy for suppressing high voltage P3−O1 phase transition of O3-$NaMn_{0.5}Ni_{0.5}O_2$ layered cathode [J]. Chemical Engineering Journal, 2022, 431: 133454.

[34] ZHANG Shi-guang, LI Xin-yan, SU Yun, YANG Yang, YU Hao, WANG Hai-bo, ZHANG Qing, LU Ya-xiang, SONG Da-wei, WANG Shan-feng, ZHANG Qing-hua, RONG Xiao-hui, ZHANG Lian-qi, CHEN Li-quan, HU Yong-sheng. Four-in-one strategy to boost the performance of $Na_x[Ni,Mn]O_2$ [J]. Advanced Functional Materials, 2023, 33(36): 2301568.

[35] HONG Ning-yun, LI Jian-wei, WANG Hao-ji, HU Xin-yu, ZHAO Bin, HUA Fang, MEI Yu, HUANG Jiang-nan, ZHANG Bai-chao, JIAN Wei-shun, GAO Jin-qiang, TIAN Yuan, SHI Xi-xi, DENG Wen-tao, ZOU Guo-qiang, HOU Hong-shuai, HU Zhang-gui, LONG Zhen, JI Xiao-bo. Regulating phase transition and restraining Fe distortion at high potential window via rare earth metal incorporation on O3-type layered cathodes [J]. Advanced Functional Materials, 2024, 34(37): 2402398.

[36] WU Xue-hang, GUO Jiang-huai, WANG Da-wei, ZHONG Gui-ming, MCDONALD M J, YANG Yong. P2-type $Na_{0.66}Ni_{0.33-x}Zn_xMn_{0.67}O_2$ as new high-voltage cathode materials for sodium-ion batteries [J]. Journal of Power Sources, 2015, 281: 18−26.

[37] ZHANG Xiao-yan, ZHOU Ya-nan, YU Lian-zheng, ZHANG Si-Yuan, XING Xuan-xuan, WANG Wen-long, XU Sai-long. Suppressing multiphase transitions of an O3-$NaNi_{0.5}Mn_{0.5}O_2$ cathode by iron and magnesium co-doping towards sodium-ion batteries [J]. Materials Chemistry Frontiers, 2021, 5(14): 5344−5350.

[38] WANG Peng-fei, YAO Hu-rong, LIU Xin-yu, ZHANG Jie-nan, GU Lin, YU Xi-qian, YIN Ya-xia, GUO Yu-guo. Ti-substituted $NaNi_{0.5}Mn_{0.5-x}Ti_xO_2$ cathodes with reversible O3−P3 phase transition for high-performance sodium-ion batteries [J]. Advanced Materials, 2017, 29(19): 1700210.

[39] JIANG Chun-yu, WANG Ying-shuai, XIN Yu-hang, DING Xiang-yu, LIU Sheng-kai, PANG Yan-fei, CHEN Bao-rui, WANG Yu-song, LIU Lei, WU Feng, GAO Hong-cai. Toward high stability of O3-type $NaNi_{1/3}Fe_{1/3}Mn_{1/3}O_2$ cathode material with zirconium substitution for advanced sodium-ion batteries [J]. Carbon Neutralization, 2024, 3(2): 233−244.

[40] HWANG J Y, YU T Y, SUN Y K. Simultaneous MgO coating and Mg doping of $Na[Ni_{0.5}Mn_{0.5}]O_2$ cathode: facile and customizable approach to high-voltage sodium-ion batteries [J]. Journal of Materials Chemistry A, 2018, 6(35): 16854−16862.

[41] WANG Hai-bo, DINH Fei-xiang, WANG Yu-qi, HAN Zhen, DANG Rong-bin, YU Hao, YANG Yang, CHEN Zhao, LI Yu-qi, XIE Fei, ZHANG Shi-guang, ZHANG Hong-zhou, SONG Da-wei, RONG Xiao-hui, ZHANG Lian-qi, XU Ju-ping, YIN Wen, LU Ya-xiang, XIAO Rui-juan, SU Dong, CHEN Li-quan, HU Yong-sheng. In situ plastic-crystal-coated cathode toward high-performance Na-ion batteries [J]. Acs Energy Letters, 2023, 8(3): 1434−1444.

[42] CHEN Kang-yi, SHI Qing-mo, WANG Yue, LI Xing-hai, JIANG Ying-ying, XU Hao-ran, GUO Shi-long, ZHAO Li, DAI Chang-song. Effects of scandium doping on the electrochemical performance of cathode materials $Na_3MnTi(PO_4)_3$ for sodium-ion batteries [J]. Colloids and Surfaces A: Physicochemical and Engineering Aspects, 2023, 662: 130996.

[43] WANG Hao-ji, CHEN Hong-yi, MEI Yu, GAO Jin-qiang, NI Lian-shan, HONG Ning-yun, ZHANG Bai-chao, ZHU Fang-jun, HUANG Jiang-nan, WANG Kai, DENG Wen-tao, SILVESTER D S, BANKS C E, YASAR S, SONG Bai, ZOU Guo-qiang, HOU Hong-shuai, JI Xiao-bo. Manipulating local chemistry and coherent structures for high-rate and long-life sodium-ion battery cathodes [J]. ACS Nano, 2024, 18(2): 13150−13163.

[44] YU Yang, ZHANG Ji-cheng, GAO Rui, WONG Deniz, An Ke, ZHENG Li-rong, ZHANG Nian, SCHULZ C, LIU Xiang-feng. Triggering reversible anion redox chemistry in O3-type cathodes by tuning Na/Mn anti-site defects [J]. Energy & Environmental Science, 2023, 16(2): 584−597.

[45] PENG Bo, CHEN Yan-xu, WANG Feng, SUN Zhi-hao, ZHAO Li-ping, ZHANG Xiao-lei, WANG Wen-tao, ZHANG Gen-qiang. Unusual site-selective doping in layered cathode strengthens electrostatic cohesion of alkali-metal layer for practicable sodium-ion full cell [J]. Advanced Materials, 2022, 34(6): 2103210.

[46] FENG Sheng, ZHENG Chu-jun, SONG Zhi-YANG, WU Xiang-wei, WU Mei-fen, XU Fang-fang, WEN Zhao-yin. Boosting fast ionic transport and stability of O3-$NaNi_{1/3}Fe_{1/3}Mn_{1/3}O_2$ cathode via Al/Cu synergistically modulating microstructure for high-rate sodium-ion batteries [J]. Chemical Engineering Journal, 2023, 475: 146090.

Sc 和 Zn 双取代增强 O3-$NaMn_{0.5}Ni_{0.5}O_2$ 正极的 Na^+扩散动力学和结构稳定性

王彬彬[1]，冯伊铭[2]，罗 鑫[1]，黄 群[3]，侯子兴[1]，
吴雅琴[1]，王鹏宇[1]，齐宇阳[4]，孟庆飞[4]，韦伟峰[1]，周亮君[1]

1. 中南大学 粉末冶金国家重点实验室，长沙 410083；
2. 先导科技集团有限公司，广州 510623；
3. 中国电子科技集团公司第四十八研究所，长沙 410111；
4. 武汉中原长江科技发展有限公司，武汉 430090

摘 要：采用溶液燃烧和固态相结合的方法将 Sc 和 Zn 引入 O3-$NaMn_{0.5}Ni_{0.5}O_2$(NaMN)，研究 Sc 和 Zn 双取代对 NaMN 的 Na^+扩散动力学和结构稳定性的影响。物理化学表征表明，Sc 和 Zn 的引入拓宽 Na^+的扩散通道，削弱 Na—O 键，从而促进 Na^+的扩散。理论计算结果表明，Sc 和 Zn 双取代降低 Na^+的扩散势垒，提高材料的电导率。双取代的 $NaMn_{0.5}Ni_{0.4}Sc_{0.04}Zn_{0.04}O_2$(NaMNSZ44)正极具有高的循环稳定性，在 1*C* 下进行 200 次循环后，容量保持率为 71.2%，在 5*C* 下进行 400 次循环后，容量保持率为 54.8%。此外，与硬碳负极匹配组装的全电池具有显著的长期循环稳定性，在 1*C* 下进行 250 次循环后容量保持 64.1%。这些结果表明，Sc 和 Zn 双取代是一种改善 NaMN 的 Na^+扩散动力学和结构稳定性的有效策略。

关键词：层状氧化物正极；Sc 和 Zn 双取代；结构稳定性；Na^+扩散动力学

(Edited by Bing YANG)